



Publication Year	2021
Acceptance in OA @INAF	2022-05-31T11:27:19Z
Title	Estimating Magnetic Filling Factors from Simultaneous Spectroscopy and Photometry: Disentangling Spots, Plage, and Network
Authors	Milbourne, T. W.; Phillips, D. F.; Langellier, N.; Mortier, A.; Haywood, R. D.; et al.
DOI	10.3847/1538-4357/ac1266
Handle	http://hdl.handle.net/20.500.12386/32126
Journal	THE ASTROPHYSICAL JOURNAL
Number	920



Estimating Magnetic Filling Factors from Simultaneous Spectroscopy and Photometry: Disentangling Spots, Plage, and Network

T. W. Milbourne^{1,2} , D. F. Phillips² , N. Langellier^{1,2} , A. Mortier^{3,4} , R. D. Haywood^{2,5,20} , S. H. Saar² ,
H. M. Cegla^{6,7,21} , A. Collier Cameron⁸ , X. Dumusque⁹ , D. W. Latham² , L. Malavolta¹⁰ , J. Maldonado¹¹ ,
S. Thompson³ , A. Vanderburg¹² , C. A. Watson¹³ , L. A. Buchhave¹⁴ , M. Ceconi¹⁵ , R. Cosentino¹⁵ , A. Ghedina¹⁵ ,
M. Gonzalez¹⁵ , M. Lodi¹⁵ , M. López-Morales² , A. Sozzetti¹⁶ , and R. L. Walsworth^{17,18,19} 

¹ Department of Physics, Harvard University, Cambridge, MA 02138, USA; tmilbourne@g.harvard.edu

² Center for Astrophysics | Harvard & Smithsonian, Cambridge, MA 02138, USA

³ Astrophysics Group, Cavendish Laboratory, J.J. Thomson Avenue, Cambridge CB3 0HE, UK

⁴ Kavli Institute for Cosmology, University of Cambridge, Madingley Road, Cambridge CB3 0HA, UK

⁵ Astrophysics Group, University of Exeter, Exeter EX4 2QL, UK

⁶ Centre for Exoplanets and Habitability, University of Warwick, Coventry, CV4 7AL, UK

⁷ Department of Physics, University of Warwick, Coventry, CV4 7AL, UK

⁸ Centre for Exoplanet Science, SUPA, School of Physics and Astronomy, University of St. Andrews, St. Andrews KY16 9SS, UK

⁹ Observatoire de Genève, Université de Genève, 51 chemin des Maillettes, 1290 Versoix, Switzerland

¹⁰ Dipartimento di Fisica e Astronomia “Galileo Galilei”, Università di Padova, Vicolo dell’Osservatorio 3, I-35122 Padova, Italy

¹¹ INAF-Osservatorio Astronomico di Palermo, Piazza del Parlamento 1, I-90134 Palermo, Italy

¹² Department of Astronomy, University of Wisconsin, Madison, WI 53706-1507, USA

¹³ Astrophysics Research Centre, School of Mathematics and Physics, Queen’s University Belfast, BT7 1NN, Belfast, UK

¹⁴ DTU Space, National Space Institute, Technical University of Denmark, Elektrovej 328, DK-2800 Kgs. Lyngby, Denmark

¹⁵ INAF-Fundacion Galileo Galilei, Rambla Jose Ana Fernandez Perez 7, E-38712 Brena Baja, Spain

¹⁶ INAF-Osservatorio Astrofisico di Torino, via Osservatorio 20, I-10025 Pino Torinese, Italy

¹⁷ Department of Physics, University of Maryland, College Park, MD 20742, USA

¹⁸ Department of Electrical and Computer Engineering, University of Maryland, College Park, MD 20742, USA

¹⁹ Quantum Technology Center, University of Maryland, College Park, MD 20742, USA

Received 2021 May 17; revised 2021 July 6; accepted 2021 July 6; published 2021 October 8

Abstract

State-of-the-art radial velocity (RV) exoplanet searches are limited by the effects of stellar magnetic activity. Magnetically active spots, plage, and network regions each have different impacts on the observed spectral lines and therefore on the apparent stellar RV. Differentiating the relative coverage, or filling factors, of these active regions is thus necessary to differentiate between activity-driven RV signatures and Doppler shifts due to planetary orbits. In this work, we develop a technique to estimate feature-specific magnetic filling factors on stellar targets using only spectroscopic and photometric observations. We demonstrate linear and neural network implementations of our technique using observations from the solar telescope at HARPS-N, the HK Project at the Mt. Wilson Observatory, and the Total Irradiance Monitor onboard SORCE. We then compare the results of each technique to direct observations by the Solar Dynamics Observatory. Both implementations yield filling factor estimates that are highly correlated with the observed values. Modeling the solar RVs using these filling factors reproduces the expected contributions of the suppression of convective blueshift and rotational imbalance due to brightness inhomogeneities. Both implementations of this technique reduce the overall activity-driven rms RVs from 1.64 to 1.02 m s⁻¹, corresponding to a 1.28 m s⁻¹ reduction in the rms variation. The technique provides an additional 0.41 m s⁻¹ reduction in the rms variation compared to traditional activity indicators.

Unified Astronomy Thesaurus concepts: [Exoplanets \(498\)](#); [Radial velocity \(1332\)](#); [Exoplanet detection methods \(489\)](#); [Solar activity \(1475\)](#); [Solar active regions \(1974\)](#)

Supporting material: data behind figure

1. Introduction

State-of-the-art radial velocity (RV) searches for low-mass, long-period exoplanets are limited by the effects of stellar magnetic activity. An Earth-mass planet in the habitable zone of a Sun-like star has an RV amplitude on the order of 10 cm s⁻¹. However, stellar activity processes on host stars, such as acoustic oscillations, magnetoconvection, suppression of convective blueshift, and long-term activity cycles, can produce signals with amplitudes exceeding 1 m s⁻¹. A variety of techniques exist to mitigate the effect of these processes on the measured RVs: Chaplin et al. (2019) discuss optimal

exposure times to average out acoustic oscillations; Cegla (2019) and Meunier et al. (2017) present strategies for mitigating the effects of granulation; and Aigrain et al. (2012), Rajpaul et al. (2015), Haywood et al. (2020), Langellier et al. (2021), and numerous others discuss statistically and physically driven techniques for removing the effects of large-scale magnetic regions from RV measurements.

On timescales of the stellar rotation period, the apparent RV is modulated by three main types of active regions: dark sunspots, large bright plage, and small bright network regions. These different regions may be identified using full-disk solar images as shown in Figure 1. Milbourne et al. (2019) (hereafter referred to as MH19) found that the large-scale photospheric plage contribute differently to the solar suppression of convective

²⁰ NASA Sagan Fellow.

²¹ UKRI Future Leaders Fellow.

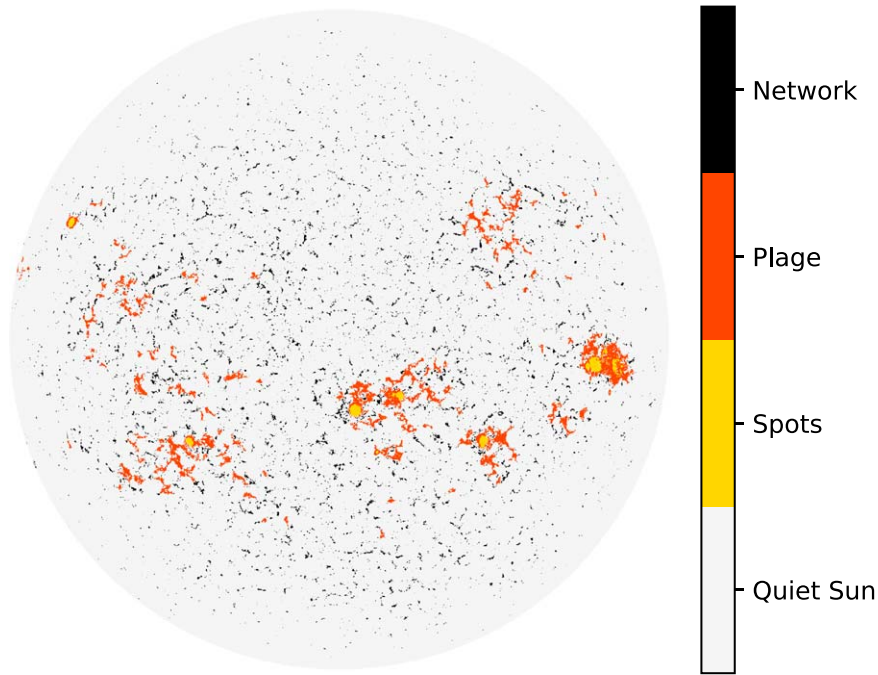


Figure 1. A representative HMI map of the three classes of active regions considered in this work. Spots, plage, and network are identified using the thresholding algorithm described by Haywood et al. (2016) and MH19, with the threshold values given by Yeo et al. (2013). This algorithm is briefly recapped in Section 2.3. Image taken 2015 January 1 at 0:0:0.00 UT.

blueshift than the smaller network. Failure to account for this different contribution leads to a significant RV shift over the 800 day span their of observations. Some of the long-term variation reported in MH19 may also be attributed to instrumental systematics: re-reducing the HARPS-N solar data with the ESPRESSO DRS (Dumusque et al. 2021; Pepe et al. 2021) reduces this shift from 2.6 ± 0.3 to 1.6 ± 0.5 m s^{-1} . However, the remaining RV shift can only be fully removed by properly accounting for network regions in the calculated activity-driven RVs. While this analysis is possible on the Sun using high-resolution full-disk images, traditional spectroscopic activity indicators, such as the Mt. Wilson S-Index (Wilson 1968; Linky & Avrett 1970) and the derivative index $\log(R'_{\text{HK}})$ (Vaughan et al. 1978; Noyes et al. 1984) do not differentiate between large and small active regions. A new activity index or combination of activity indices is therefore necessary to successfully model the suppression of convective blueshift on stellar targets.

In this work, we demonstrate a new technique using simultaneous spectroscopy and photometry to estimate spot, plage, and network filling factors and demonstrate that these filling factors may be used to model RV variations. In Section 2, we discuss the solar data used by our technique. An analytical implementation of the technique is described in Section 3 and a neural network implementation is presented in Section 4. The resulting solar filling factors, a model of the solar RVs, and possible applications to stellar targets are analyzed in Section 5.

2. Measurements

2.1. HARPS-N/Mt. Wilson Survey

We use the HARPS-N solar telescope (Dumusque et al. 2015; Phillips et al. 2016) measurements of the S-index, as described in MH19 and Collier Cameron et al. (2019). The S-index quantitatively represents activity-driven chromospheric

re-emission in the Calcium II H and K lines. The presence of spots, plage, and network all increase the S-index. The solar telescope takes exposures every five minutes while the Sun is visible. Each measurement of the S-index has an average precision of 2.5×10^{-4} or a fractional uncertainty of 0.0016.

Note that HARPS-N solar telescope observations began in mid-2015. To cover the rest of the solar cycle, we use data from the Mt. Wilson S-index survey, as presented by Egeland et al. (2017). Observations from the two instruments overlap between 2015 July and 2016 February (JD 2457222 and JD 2457444), allowing us to combine these time series. The solar telescope data set is rescaled so that the points in the overlapping time interval have the same mean and variance as the Mt. Wilson data from the same time interval, as described in Haywood et al. (2020). The resulting combined data set is shown in the top panel of Figure 2.

2.1.1. HARPS-N Solar RVs

We use the HARPS-N solar telescope’s measurements of the solar RVs to assess our ability to model realistic RV variations using our estimated filling factors²² (Phillips et al. 2016; Collier Cameron et al. 2019; Dumusque et al. 2021) as well as our estimated values derived from the linear and MLP techniques. The HARPS-N RVs used in this work span the period from 2015 July to 2017 October, with exposures taken every five minutes while the Sun is visible. Each RV measurement has an average precision of 23 cm s^{-1} .

2.2. SORCE

We use the Total Irradiance Monitor (TIM) onboard the Solar Radiation and Climate Experiment (SORCE; Kopp & Lawrence 2005; Kopp et al. 2005; Rottman 2005) to measure

²² We use publicly available HARPS-N solar telescope observations reduced using the most recent ESPRESSO pipeline, available at <https://dace.unige.ch/Sun/>.

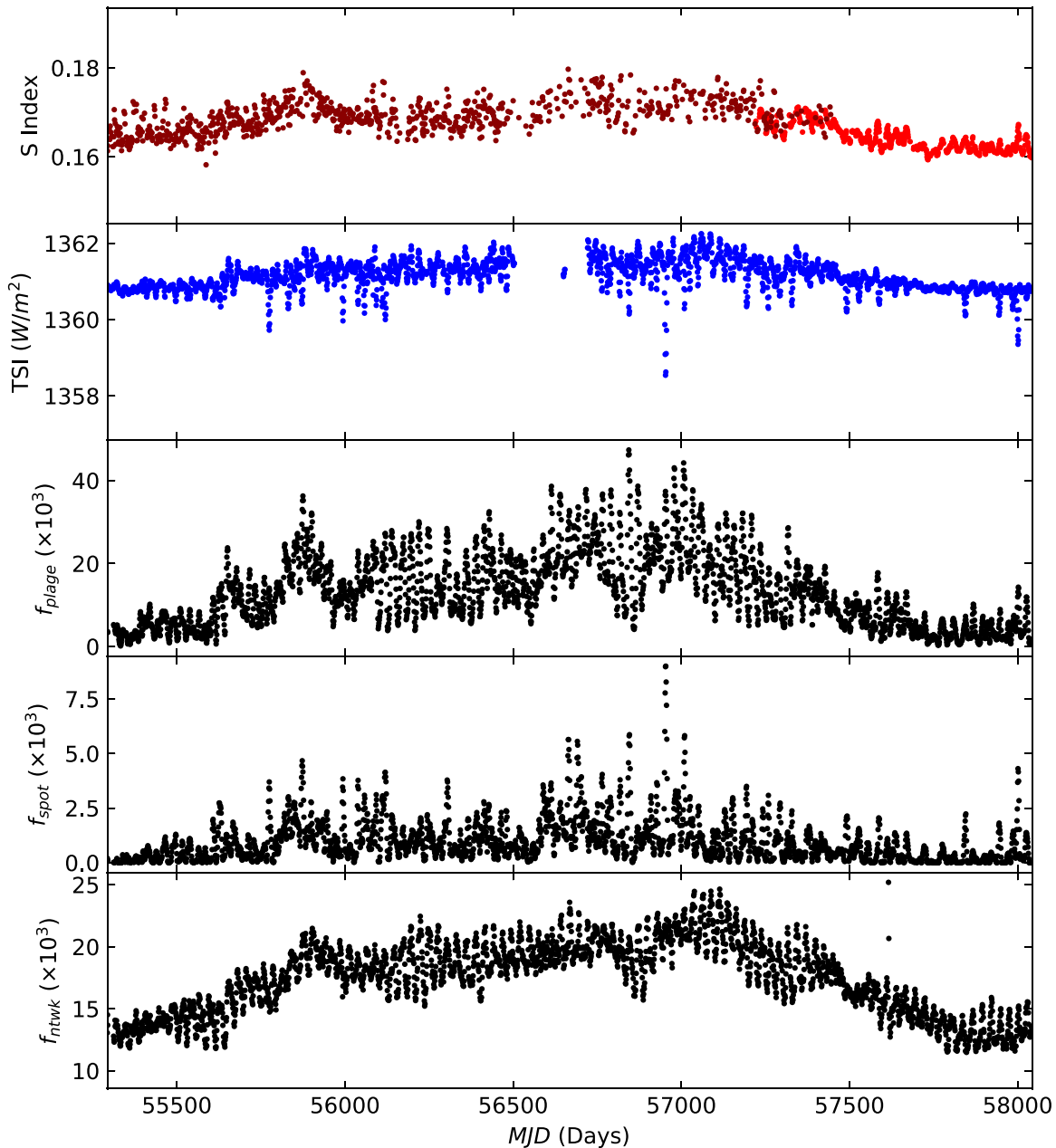


Figure 2. Time series of solar observations used in this work. From top to bottom: Mt. Wilson and HARPS-N solar telescope observations of the calcium S-index (red); Total Solar Irradiance (TSI) from SORCE/TIM (blue); and SDO/HMI plage, spot, and network filling factors (black). Note the consistent overall shapes of the S-index, TSI, and bright filling factors, and that dips in the TSI are coincident with peaks in the spot filling factor. Observations are taken between 2010 April through 2017 October. Note the two different reds used in the S-index plot: the darker red points correspond to measurements by Mt. Wilson and bright red points are from the HARPS-N solar telescope. Note that due to an instrumental anomaly, no TSI data are available from SORCE/TIM from mid-July 2013 until March 2014—we therefore do not use any times in this period in our analysis (Kopp & Lawrence 2005; Kopp et al. 2005).

(The data used to create this figure are available.)

photometry for the whole solar cycle. The total solar irradiance (TSI) is the solar analog of the light curves obtained by Kepler, K2, TESS, and CHEOPS (Borucki et al. 2010; Howell et al. 2014; Ricker et al. 2014; Cessa et al. 2017), though the Sun’s proximity means it can be observed continuously over much longer periods. The TIM level 3 data products are averaged over 6 hr, with a precision of 0.005 W m^{-2} .

We expect the overall brightness of the Sun to vary with stellar cycle. Its relative brightness increases with the presence

of plage and network and decreases with the presence of spots. This modulation makes the TSI, and stellar light curves in general, useful tools for isolating the effects of stellar magnetic activity (Aigrain et al. 2012). The time series of the TSI is shown in the second panel of Figure 2.

2.3. SDO

We use images from the Helioseismic and Magnetic Imager (HMI) instrument onboard the Solar Dynamics Observatory

(SDO, Pesnell et al. 2012; Schou et al. 2012; Couvidat et al. 2016) to independently calculate solar filling factors. HMI measures the 6173.3 Å iron line at six points in wavelength space using two polarizations. From these measurements, they reconstruct the Doppler shift and magnetic field strength along with the continuum intensity, line width, and line depth at each point on the solar disk.

Spots, plage, and network are identified on HMI images using a simple thresholding algorithm:

1. An HMI pixel is considered magnetically active if the radial component of the magnetic field is over three times greater than the expected noise floor: $|B_r| > 3\sigma_{B_r}$.
2. Active pixels below the intensity threshold of Yeo et al. (2013), such that $I < 0.89I_{\text{quiet}}$, are labeled as spots. Here, I_{quiet} is the average intensity of inactive pixels on a given image.
3. Active regions exceeding the above intensity threshold that span an area >20 microhemispheres (that is, 20 parts per million of the visible hemisphere), or 60 Mm^2 , are labeled as plage.
4. Active regions exceeding the intensity threshold that span an area <20 microhemispheres are labeled as network.

These calculations are explained in further detail in MH19. The resulting filling factors for each feature are plotted in the bottom three panels of Figure 2. We use one HMI image taken every four hours in our analysis. The photon noise at disk center for the magnetograms and continuum intensity for these HMI images are $\sigma_{B_r} = 8 \text{ G}$ and $\sigma_{I_c} = 0.01\%$, respectively (Couvidat et al. 2016). This corresponds to uncertainties $<0.1\%$ in the resulting magnetic filling factors.

Since SDO/HMI allows us to perform precise, direct, independent measurements of the three filling factors of interest, we use these results as the “ground truth” in our analysis.

An SDO analog does not exist for non-solar stars, so if we wish to determine feature-specific filling factors of stellar targets we must make indirect estimates of the filling factors using spectroscopic and photometric data. In the next section, we discuss two processes to do so. To mitigate the effects of acoustic oscillations, granulation, and other short-timescale activity processes, we take daily averages of each set of observations used in our analysis. We also interpolate the HARPS-N/Mt. Wilson observations, SORCE/TIM observations, and SDO/HMI filling factors onto a common time grid of one observation each day, when all three instruments have measurements.

3. Methods

In this section, we present analytical and neural net implementations of a technique to determine the spot, plage, and magnetic filling factors using only spectroscopic and photometric data. The analytical implementation (hereafter referred to as the “linear technique”) only requires knowledge of the star’s distance and radius along with estimates of the spot and plage/network temperature contrasts and the quiet star effective temperature. The neural net implementation infers these parameters from the data, and therefore only requires spectroscopic and photometric observations of the target. This technique can therefore be used to estimate filling factors without prior knowledge of the filling factors from full-disk images. Furthermore, if the resulting filling factors are only

being used to model activity-driven RV variations, only time series correlated with the spot, network, and plage filling factors are needed, further simplifying the required knowledge of the star.

3.1. Filling Factor Modelling: Linear Technique

3.1.1. Modelling Irradiance Variations Using Filling Factors

In MH19, the authors reproduce the observed TSI using a linear combination of the spot and plage filling factors. Following Meunier et al. (2010a), they use the SDO/HMI-derived plage and spot filling factors and assume that the solar irradiance follows the Stefan-Boltzmann law for blackbodies:

$$TSI = \mathcal{A}\sigma[(1 - f_{\text{spot}} - f_{\text{bright}})T_{\text{quiet}}^4 + f_{\text{spot}}(T_{\text{quiet}} + \Delta T_{\text{spot}})^4 + f_{\text{bright}}(T_{\text{quiet}} + \Delta T_{\text{bright}})^4] \quad (1)$$

where σ is the Stefan-Boltzmann constant, $\mathcal{A} = (R_{\odot}/1 \text{ au})^2$ is a geometrical constant relating the energy emitted at the solar surface to the energy received at Earth, T_{quiet} is the quiet Sun temperature, ΔT_{spot} and ΔT_{bright} are the effective temperature contrasts of spots and plage/network regions, and f_{spot} and f_{bright} are the HMI spot and plage/network filling factors. Expanding as a power series yields the following approximation:

$$TSI \approx \mathcal{A}\sigma T_{\text{quiet}}^4 \left(1 + 4 \frac{\Delta T_{\text{spot}}}{T_{\text{quiet}}} f_{\text{spot}} + 4 \frac{\Delta T_{\text{bright}}}{T_{\text{quiet}}} f_{\text{bright}} \right) \quad (2)$$

In MH19, the authors show that HMI observations of filling factors may be used to reproduce SORCE TSI given temperature contrasts for plage/network features and spots and the effective temperature of the quiet Sun. In this work, we invert the process and use the resulting effective temperatures of each type of active region, along with the correlations between the TSI, S index, and filling factors demonstrated in MH19 to reproduce the observed magnetic filling factors for each type of active region. The potential stellar applications of this technique are discussed in more detail in Section 5.3.

We begin by fitting the SORCE TSI to Equation (2) using the SDO/HMI measurements of f_{spot} and f_{bright} . This fit yields $T_{\text{quiet}} = 5769.85 \pm 0.01 \text{ K}$, $\Delta T_{\text{spot}} = -525 \pm 8 \text{ K}$, and $\Delta T_{\text{bright}} = 46.1 \pm 0.5 \text{ K}$. Also note that the solar radius varies as a function of wavelength. To be consistent with HMI, we use $R_{\odot} = 695,982 \pm 13 \text{ km}$, the solar radius measured at 6,173.3 Å (Rozelet et al. 2015).

3.1.2. Differentiating Bright and Dark Regions

The brightness of a Sun-like star may be modulated by the long-term stellar activity cycle (e.g., the 11 year solar cycle). Since $\Delta T_{\text{bright}} > 0$ and $\Delta T_{\text{spot}} < 0$, we see from Equation (2) that TSI variations (on timescales of the rotation period) below the value expected from the activity cycle must be the result of spots. Since the Sun is plage-dominated (that is, $f_{\text{bright}} > 100f_{\text{spot}}$, as shown in Shapiro et al. 2016, MH19, and Figure 2), plage and network are the primary source of variation of the TSI and S-index, with spots making negligible contributions to the variability of the irradiance on timescales of the solar cycle. This is also visible in comparing the plots of the TSI, S-index, f_{plage} , and f_{ntwk} shown in Figure 2, and is also

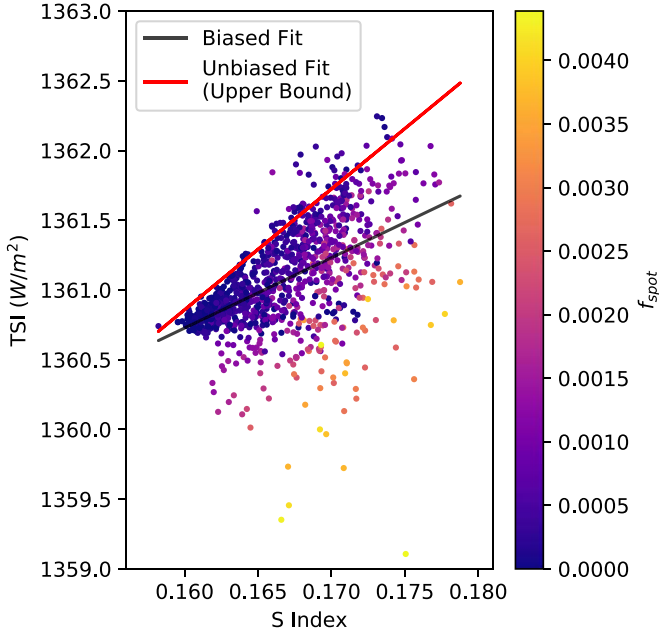


Figure 3. A plot of the SORCE TSI vs. the HARPS-N/Mt. Wilson S-index. The color of each point corresponds to the value of f_{spot} . We see that the S-index is highly correlated with the TSI, as expected. We may use this correlation to estimate the plage/network filling factors on the Sun. However, increased spot coverage results in a lower TSI value for a given S-index, which will bias our estimate of the bright region filling factor. This, in turn, will result in a less accurate estimate of the spot filling factor. The black line shows the result of the straightforward linear fit of the TSI and S-index, which is biased as described above. To isolate the plage and network-driven TSI variations, we find the 50% most densely clustered points in the above scatter plot and fit a line to the upper boundary of this region. (This choice in point density is arbitrary, but the resulting best-fit line is robust to variations in this parameter.) The resulting fit line, shown in red, is unbiased by the presence of spots.

discussed in detail by MH19. We may therefore use a linear transformation of the S-index to provide an initial estimate of f_{bright} and then use the TSI to estimate f_{spot} . The full calculation is as follows:

(1) We begin by assuming that the S-index is directly proportional to the total plage and network filling factor (that is, $f_{\text{bright},1} = m_1 S_{\text{HK}} + b_1$), and that the plage and network are the dominant drivers of TSI variation. Our first estimate of the spot filling factor is therefore $f_{\text{spot},1} = 0$. We then estimate the values of m_1 and b_1 by fitting the TSI as a linear transformation of the S-index:

$$TSI_{\text{fit},1}(m_1, b_1) = \mathcal{A}\sigma T_{\text{quiet}}^4 \left(1 + 4 \frac{\Delta T_{\text{bright}}}{T_{\text{quiet}}} (m_1 S_{\text{HK}} + b_1) \right). \quad (3)$$

Note that we have included the physical constants for normalization though they are degenerate with the fit parameters.

It is not sufficient to perform a simple linear fit to the TSI and S index. In the above step, we model the activity-driven variations of the TSI due to the presence of bright regions. However, as shown in Figure 3, the presence of spots produces scatter in this relationship. This scatter is in one direction: as f_{spot} increases, the observed TSI for a given value of the S-index decreases. To isolate the activity-driven TSI variations due to f_{bright} , we determine the 50% most densely clustered points in Figure 3 and fit the upper boundary of this region. The best-fit line of this upper bound gives us the values of m_1 and b_1 used above.

Table 1

Best-fit Parameters for the Linear Filling Factor Estimation Technique

m_1	2.02 ± 0.07
b_1	-0.31 ± 0.01
a_2	0.9912 ± 0.0008
m_2	2.072 ± 0.002
b_2	-0.3169 ± 0.0003

Note. As expected, m_1 and m_2 are consistent within error bars, as are b_1 and b_2 . Similarly, a_2 is very close to 1, as expected.

(2) Next, we assume any deviation from the fit above is driven by spots, which are not included in this model. We then make a second estimate of the spot filling factor, $f_{\text{spot},2}$, from the residuals to the above fit:

$$f_{\text{spot},2} = \begin{cases} \frac{TSI - TSI_{\text{fit},1}(m_1, b_1)}{4\mathcal{A}\sigma\Delta T_{\text{spot}}T_{\text{quiet}}^3}, & TSI - TSI_{\text{fit},1} \leq 0 \\ 0, & TSI - TSI_{\text{fit},1} > 0. \end{cases} \quad (4)$$

Essentially, any point below the line of best fit in Figure 3 is assumed to be due to spot-driven brightness variations. This increases the importance of avoiding spot-driven biases in Step 1. If a simple linear fit is used in Step 1 instead of the fit to the upper boundary described above, the presence of spots will reduce the slope of the best-fit line, which will result in an artificially reduced f_{bright} value, and will also exclude real spot-driven variations from our calculation of $f_{\text{spot},2}$.

(3) We determine our final estimate of f_{bright} and f_{spot} by fitting the following expression to the TSI:

$$TSI_{\text{fit},2} = \mathcal{A}\sigma T_{\text{quiet}}^4 \left(1 + 4 \frac{\Delta T_{\text{spot}}}{T_{\text{quiet}}} (a_2 f_{\text{spot},2}) + 4 \frac{\Delta T_{\text{bright}}}{T_{\text{quiet}}} (m_2 S_{\text{HK}} + b_2) \right). \quad (5)$$

where our estimated values of f_{bright} and f_{spot} are given by

$$f_{\text{bright}} = m_2 S_{\text{HK}} + b_2 \quad (6)$$

$$f_{\text{spot}} = a_2 f_{\text{spot},2} \quad (7)$$

and the parameters a_2 , m_2 , and b_2 are determined by the above fit. The resulting best-fit parameters derived from the solar case are given in Table 1. Note that we do not expect m_2 and b_2 to be very different from the parameters m_1 and b_1 found previously, nor do we expect a_2 to be very different from 1. However, since we exclude any negative residuals from our estimate of f_{spot} in Step 2 above, we perform this final fit in case this excluded information changes the best-fit parameters in any way.

As previously noted, this technique only requires knowledge of the star's distance and radius, along with estimates of the spot and plage/network temperature contrasts and the quiet star effective temperature—this means that it can be used to estimate filling factors without prior knowledge of the filling factors from full-disk images. If the plage and network features are only being used to decorrelate activity-driven RV variations, only time series correlated with the spot, network, and plage filling factors are needed, and the above terms may be absorbed into the fit coefficients in Equations (3) and (5)—this is discussed further in Section 5.3.

3.1.3. Differentiating the Network and Plage Filling Factor

In the discussion above, we extract f_{bright} , the combined plage and network filling factor. However, we may consider these two separately by adding a network term to Equation (1):

$$\begin{aligned} TSI = \mathcal{A}\sigma & [(1 - f_{\text{spot}} - f_{\text{plage}} - f_{\text{ntwk}})T_{\text{quiet}}^4 \\ & + f_{\text{spot}}(T_{\text{quiet}} + \Delta T_{\text{spot}})^4 \\ & + f_{\text{plage}}(T_{\text{quiet}} + \Delta T_{\text{plage}})^4 \\ & + f_{\text{ntwk}}(T_{\text{quiet}} + \Delta T_{\text{ntwk}})^4]. \end{aligned} \quad (8)$$

Fitting this equation to the TSI, this time using the SDO observed filling factors as inputs, reveals that the plage and network have distinct effective temperatures, $\Delta T_{\text{plage}} = 32 \pm 1K$ and $\Delta T_{\text{ntwk}} = 79 \pm 2K$. This is consistent with the intensity maps produced by HMI, which show that network regions are, on average, indeed brighter than plage. These temperature contrasts are necessary for separating the plage and network contributions to the filling factor.

Setting Equation (1) equal to Equation (8) and expanding as a power series, we find

$$f_{\text{bright}} \Delta T_{\text{bright}} \approx f_{\text{plage}} \Delta T_{\text{plage}} + f_{\text{ntwk}} \Delta T_{\text{ntwk}}.$$

Since areas are additive, we also expect

$$f_{\text{bright}} = f_{\text{plage}} + f_{\text{ntwk}}.$$

Combining these equations and solving for f_{ntwk} and f_{plage} in terms of f_{bright} yields the following expressions:

$$f_{\text{ntwk}} = \frac{\Delta T_{\text{plage}} - \Delta T_{\text{bright}}}{\Delta T_{\text{plage}} - \Delta T_{\text{ntwk}}} f_{\text{bright}} + \mathcal{B}, \quad (9)$$

and

$$f_{\text{plage}} = \frac{\Delta T_{\text{bright}} - \Delta T_{\text{ntwk}}}{\Delta T_{\text{plage}} - \Delta T_{\text{ntwk}}} f_{\text{bright}} - \mathcal{B}. \quad (10)$$

Note the prefactors for each estimate, which simply rescale the brightness contributions of each class of active region to account for the different effective temperatures. Also note the offset \mathcal{B} in our estimate of f_{plage} : this accounts for the fact that f_{plage} goes to 0 at solar minimum, while f_{ntwk} has a basal value at solar minimum. In this analysis, the value of \mathcal{B} may be found from the expected value of f_{bright} at solar minimum:

$$\mathcal{B} = \frac{\Delta T_{\text{bright}} - \Delta T_{\text{ntwk}}}{\Delta T_{\text{plage}} - \Delta T_{\text{ntwk}}} \min(f_{\text{bright}}). \quad (11)$$

Determining this offset therefore requires TSI and S index observations taken at solar minimum, which may increase the observational load associated with this technique. However, modeling the effects of network on the activity-driven solar RV variations only requires a quantity *correlated with* f_{plage} . The value of this offset is therefore unimportant for our purposes.

3.2. Filling Factor Modelling: Machine Learning Technique

While machine learning techniques are predicatively powerful, their black-box nature makes them not physically explanatory, and therefore not necessarily useful for some scientific applications. However, the existence of a clear causal connection between the S-index, TSI, and filling factors makes

Table 2

Hyperparameter Values for MLP Filling Factor Calculation as Optimized from Cross-validation

Hidden Layer Sizes	α	β
(64, 64)	0.0001	0.001

Note. Here α gives the L_2 regularization parameter and β is the learning rate.

machine learning a strong candidate for the problem of estimating feature-specific magnetic filling factors from spectroscopic and photometric information. We already know the physics connecting these variables, and can therefore have machine learning “discover” and refine the relationships found above. A neural network used as a universal function approximator (Cybenko 1989) may be able to determine subtle details of these relationships that are not incorporated into our linear model such as the different effects of network versus plage, how underlying spatial distributions of active regions affect the resulting filling factors and activity indicators, and the correlations between spots and plage.

We therefore compare the linear technique discussed in the previous section with a type of neural network known as a Multilayer Perceptron (MLP, Hinton 1989). The MLP consists of an input layer, several fully connected hidden layers, and an output layer. It is one of the simplest neural networks that may be used as a universal function approximator, making it ideal for this application. We implement the MLP using the MLPRegressor class in the `scikit-learn` package in Python (van Rossum 1995; Pedregosa et al. 2011).

We train the MLP using the TSI and S-index inputs and using the SDO plage, spot, and network filling factors as outputs. Of the total available data (taken over the whole solar cycle), 75% is used for training, with 25% set aside to test the performance of the trained network. The MLP uses two hidden network layers, each with 64 neurons. We optimized the size and number of these layers as well as the L_2 regularization parameter, α , which combats overfitting by constraining the size of the fit parameters as measured with an L_2 norm, and the learning rate, β , which controls the step-size in the parameter space search using five-fold cross-validation. That is, we randomly shuffled the training data and divided it into five groups. We trained the network on four of these groups and then tested the network on the remaining group. We repeated this process using each of the five groups as a test set to mitigate the effects of overfitting on our network and then repeated the entire five-fold process using each combination of network parameters to determine which combination of hyperparameters resulted in the best performance. The resulting values are summarized in Table 2. The network was optimized to minimize square error using a stochastic gradient descent algorithm and was trained for a maximum of 10^4 steps (though the algorithm may stop training earlier once the network converges).

Note that we may also use this MLP approach to fit the solar RVs directly using the TSI and S-index without first computing magnetic filling factors. In Section 5.2, we compare a direct MLP fit of this form to RV models derived from our estimated filling factors to determine if there is any additional RV information in the TSI and S-index which is not incorporated into our filling factor estimates.

3.3. Radial Velocity Modelling

In MH19, the authors found that the HARPS-N solar radial velocities were well-represented by a linear combination of Δv_{conv} , the suppression of convective blueshift, and Δv_{phot} , the photometric velocity shift due to bright and dark active regions breaking the symmetry of the solar rotational profile:

$$RV = A_1 \Delta v_{\text{phot}} + B_1 \Delta v_{\text{conv}} + RV_0. \quad (12)$$

Here, we see if we can perform a similar reconstruction using our estimates of the magnetic filling factors. Since the presence of active regions drives the suppression of convective blueshift, we expect the Δv_{conv} to be proportional to the spot, plage, and network filling factors. Based on the results of MH19, we also expect network and plage regions to have different contributions to Δv_{conv} . We therefore model the suppression of convective blueshift as:

$$\Delta v_{\text{conv}} = Bf_{\text{spot}} + Cf_{\text{plage}} + Df_{\text{network}} + E. \quad (13)$$

While plage and network occupy a greater area than spots on the Sun and therefore dominate the suppression of convective blueshift, the higher brightness contrast of spots means that they drive the photometric RV shift, Δv_{phot} . We expect Δv_{phot} to scale with number and size of the spots rotating across the solar surface. However, we also expect a phase lag between f_{spot} and Δv_{phot} . For a single spot moving across the solar disk, f_{spot} is at its maximum value when the spot is on the center of the solar disk. However, the absolute value of Δv_{phot} is maximized when the spot is at the solar limb, rotating toward or away from the observer, and is zero when the spot is at disk center. We therefore expect Δv_{phot} to also depend on the derivative of the filling factor with respect to time:

$$\Delta v_{\text{phot}} \propto f_{\text{spot}} \times \left(\frac{df_{\text{spot}}}{dt} \right). \quad (14)$$

Note that this formulation mirrors the FF' method developed by Aigrain et al. (2012).

By combining Equations (12), (13), and (14), we therefore produce a model of the solar RVs based on our estimated feature-specific magnetic filling factors:

$$RV = Af_{\text{spot}} \left(\frac{df_{\text{spot}}}{dt} \right) + Bf_{\text{spot}} + Cf_{\text{plage}} + Df_{\text{network}} + RV_0. \quad (15)$$

Note that the offset E in Equation (13) has been absorbed into RV_0 .

Fitting to the HMI-observed filling factors reduces the HARPS-N solar RV residuals from 1.64 to 0.91 m s^{-1} as shown in Table 5. In comparison, the usual technique of simply decorrelating the S-index from the RV measurements (i.e., fitting $RV = AS_{\text{HK}} + B$) results in an rms of only 1.10 m s^{-1} , indicating that spots, plage, and network regions have different contributions to the S-index and have different effects on the suppression of convective blueshift (Meunier et al. 2010b, Figure 7).

Repeating this fit with both our linear and MLP estimates of f_{spot} , f_{ntwk} , and f_{plage} reduces the rms RV to 1.04 m s^{-1} and to 1.02 m s^{-1} , respectively. This implies that, while our estimates are highly correlated with the true values of the filling factors, there is additional information in the true filling factors that is not captured by either technique, resulting in less precise

estimates of the convective blueshift and photometric RV shifts. Interestingly, while the linear filling factor estimates cannot distinguish the RV contributions of the spots and network, as discussed above, the linear and MLP estimates result in similar rms RVs. The fact that the linear estimates reduce the rms RVs below the level obtained from the S-index despite this limitation highlights the importance of spots in our models of activity-driven RVs.

4. Results

4.1. Spot, Plage, and Network Filling Factors

Figure 4 shows that both the linear and MLP-based techniques successfully reproduce the directly observed values of f_{spot} , f_{plage} , and f_{ntwk} . Figure 5 shows the same information as Figure 4, but for three 230 day regions taken in the middle of the solar cycle, at solar maximum, and at solar minimum. We see that, again, both the linear and MLP techniques are able to reproduce the SDO-measured values of f_{spot} , f_{plage} , and f_{ntwk} at all points in the stellar activity cycle on these timescales.

In Table 6, we list the Pearson correlation coefficients between the HMI-derived filling factors and our estimates from the linear and MLP techniques. (For the sake of consistency, note that for both the linear and MLP estimates, we compute correlation coefficients only for results generated using the fraction of data reserved for testing the MLP.) We see that both techniques reproduce the information contained in the HMI filling factors, with the MLP performing slightly better than the linear model on all three filling factors. This may indicate that there is some additional information about the filling factors present in the TSI and S-index observations that is not being used by the linear technique. However, given the high degree of correlation produced by both techniques, we can use both estimates of the magnetic filling factors to reduce the effects of activity on observed RVs.

4.2. Solar Radial Velocities

We then fit the HARPS-N solar telescope RVs to Equation (15) using the directly measured SDO filling factors. The results of each fit are given in Table 7. Note that since the linear estimates of f_{bright} , f_{ntwk} , and f_{plage} are linear transformations of the S-index, as shown in Equations (6), (9), and (10), we require $D = 0$ to avoid degeneracies when using the filling factor estimates derived from the linear technique. Fitting the linear estimated filling factors to Equation (15) without this constraint is equivalent to fitting to $RV = Af_{\text{spot}} \left(\frac{df_{\text{spot}}}{dt} \right) + Bf_{\text{spot}} + C'S_{\text{HK}} + D'S_{\text{HK}} + E'$. We therefore set $D = 0$ to avoid having degeneracies between C and D in our fit. No such constraint on D is necessary when considering the SDO or MLP filling factors.

To ensure our fit is indeed reproducing the suppression of convective blueshift and the photometric RV shift, as expected, we compare the relevant terms of Equation (15) to the SDO/HMI estimates of these RV perturbations, as calculated in MH19. In Tables 3 and 4, we compare the estimates of Δv_{conv} and Δv_{phot} computed from Equations (13) and (14) using the filling factors measured by SDO and estimated using the linear and MLP techniques to the values of Δv_{conv} and Δv_{phot} derived from HMI observations in Haywood et al. (2016) and MH19. We see that all of the estimated values of Δv_{conv} are highly correlated with the HMI-derived velocities. Our estimates of